Computers and Fluids 139 (2016) 233–247

Contents lists available at ScienceDirect

Computers and Fluids

journal homepage: www.elsevier.com/locate/compfluid

A numerical analysis of the nodal Discontinuous Galerkin scheme via Flux Reconstruction for the advection-diffusion equation

Jerry Watkins*, Kartikey Asthana, Antony Jameson

Department of Aeronautics and Astronautics, Stanford University, CA 94305, USA

ARTICLE INFO

Article history:
Received 11 December 2015
Revised 7 September 2016
Accepted 11 September 2016
Available online 12 September 2016

Keywords:
High-order
Flux Reconstruction
Discontinuous Galerkin
Advection-diffusion
CFL
Dispersion

ABSTRACT

A von Neumann analysis of the Flux Reconstruction (FR) formulation is performed for the linear advection-diffusion equation to investigate the stability, dissipation and dispersion associated with the nodal Discontinuous Galerkin (DG) scheme. We show that the maximum stable time step for advection-diffusion is stricter than that for pure-advection or pure-diffusion individually. However, the simple harmonic sum of the maximum stable time steps for advection and diffusion provides a suitable estimate for the linear advection-diffusion and Navier–Stokes equations on unstructured, tensor product elements. The estimates are accurate within 50% error on all test cases and are conservative on tests with Cartesian grids but not always on unstructured grids. We show that the CFL limit is strongly influenced by the choice of interface fluxes and, in general, the limit for a scheme using centered values is much higher than that which has one-sided values. We also verify that schemes with centered values produce less error for well resolved solutions while schemes with one-sided values produce less error for solutions that are under-resolved.

1. Introduction

The increased popularity of high-order methods in computational fluid dynamics (CFD) has led to significant advances in the simulation of unsteady, vortex dominated flows. These methods employ higher than second order spatial discretization and are capable of capturing important time-dependent flow features that popular second order methods tend to obscure. Discontinuous Galerkin (DG) methods [1,2] have been the focal point of recent efforts in developing high-order CFD codes which solve the Navier–Stokes equations because of their ability to simulate flows around complex geometries. In particular, collocation based nodal DG [3] and spectral difference (SD) [4,5] methods have been widely adopted because of their simplicity. In 2007, Huynh [6] proposed a Flux Reconstruction (FR) approach for tensor-product elements that provides a generalized differential framework for recovering both the nodal DG and SD schemes for linear advection. In 2009, he further extended this framework to diffusion problems [7]. Since then, a proof of linear stability for a specific class of FR schemes called the energy stable FR (ESFR) schemes [8] has been developed along with theory on non-linear stability and the role of aliasing errors [9,10]. The FR schemes have also been successfully extended to triangular [11,12] and tetrahedral [13] elements. Other frameworks such as the Correction Procedure via Reconstruction (CPR) [14] have been proposed that unify the FR and the Lifting Collocation Penalty (LCP) [15] formulations.

Numerical analysis of DG methods has primarily relied on functional analysis and spectral decomposition. The primary tool for analyzing dissipation and dispersion properties has been Fourier (von Neumann) analysis. In the case of linear advection, Hu et al. [16] have shown that the Pth order DG scheme results in one physical mode and P spurious or parasitic modes which dampen out quickly for an upwind flux but remain indefinitely for a centered flux. Recently, Moura et al. [17] have shown that these spurious modes, in fact, replicate the behavior of the physical mode. They also provide estimates of the largest wavenumber that can be accurately resolved within a set tolerance for Burgers turbulence. In the asymptotic limit of small wavenumber $kh \to 0$, Ainsworth [18] proved that for a fixed mesh of spacing h, dissipation and dispersion errors decay at an exponential rate when $2P+1 \approx \kappa kh$ where k is the wavenumber and $\kappa > 1$ is some constant. Toulorge et al. [19] have obtained CFL estimates on triangles through von Neumann analysis of the fully discrete equation for Runge–Kutta DG (RKDG) type schemes. In the case of the FR formulation, Vincent et al. [20] applied Fourier analysis to study the ESFR schemes for linear advection and were able to identify the '$c+$' scheme that offers the highest CFL limit for a given polynomial order while Asthana et al. [21] have been able to derive a new set of linearly

* Corresponding author.
E-mail addresses: watkins2@stanford.edu (J. Watkins), kasthana@stanford.edu (K. Asthana), jameson@baboon.stanford.edu (A. Jameson).

http://dx.doi.org/10.1016/j.compfluid.2016.09.013
0045-7930/

stable schemes which have minimal dissipation and dispersion error.

In this paper, we perform Fourier analysis of the FR formulation for the linear advection-diffusion equation. We investigate stability, dissipation and dispersion over the entire range of resolvable wavenumbers to develop an understanding of how FR behaves when the flow features are under-resolved. Our analysis focuses on different interface flux formulations of the nodal DG scheme on Gauss–Legendre points although the same technique can be applied to any scheme within the FR formulation. In pursuit of an accurate, stable time step, we provide a method for estimating the maximum stable time step for the linear advection-diffusion and Navier–Stokes equations on unstructured, tensor product elements.

The paper is formatted as follows. Section 2 introduces the semi-discrete advection-diffusion equation for FR and discusses the dissipation and dispersion properties associated with nodal DG. Section 3 derives a measure of relative error in order to compare schemes on the basis of wave-propagation error. In Section 4, the fully discrete advection-diffusion equation and its stability criteria is used to compare the CFL restrictions of different schemes. A conservative prediction method for the maximum physical time step is proposed and extended to multidimensional tensor product elements for the Navier–Stokes equations. Lastly, Section 5 provides 1D and 2D numerical tests in order to verify the results found in the previous sections.

2. Fourier (Von Neumann) analysis

We begin by demonstrating that Fourier analysis provides a purely element-local description of the 1D semi-discrete linear advection-diffusion equation. The derived linear dynamical system can then be solved analytically to obtain the analytical solution to the semi-discrete equation. The stability, dissipation and dispersion properties of any FR scheme follow directly from the corresponding eigensolutions [22]. This section concludes with a short discussion on the dissipation and dispersion error of the nodal DG scheme on Gauss–Legendre points for the advection-diffusion equation.

2.1. Problem specification

Consider the 1D linear advection-diffusion equation,

$$\frac{\partial u}{\partial \hat{t}} + \hat{a}\frac{\partial u}{\partial \hat{x}} = \hat{b}\frac{\partial^2 u}{\partial \hat{x}^2}, \qquad \hat{x} \in \mathbb{R}, \qquad \hat{t} > 0, \tag{1}$$

where $\hat{a} \in \mathbb{R}$ is the constant wavespeed and $\hat{b} > 0$ is the diffusion coefficient. A periodic initial condition is introduced as an isolated Fourier component, $u(\hat{x}, 0) = \exp(i\hat{k}\hat{x})$, where $\hat{k} > 0$ is the wavenumber. Using h as the length scale and $h^2/\hat{b}$ as the time scale, Eq. (1) and the initial condition can be nondimensionalized as,

$$\begin{aligned} &\frac{\partial u}{\partial t} + a\frac{\partial u}{\partial x} = \frac{\partial^2 u}{\partial x^2}, \qquad x \in \mathbb{R}, \qquad t > 0, \\ &u(x, 0) = \exp(ikx), \end{aligned} \tag{2}$$

where the nondimensional parameters are $x = \hat{x}/h$, $t = \hat{t}\hat{b}/h^2$, $k = \hat{k}h$, and $a = \hat{a}h/\hat{b}$.

Following a traditional nodal finite element method, the domain is partitioned into non-overlapping elements, $\Omega = \bigcup_n \Omega_n$ where $\Omega_n = \{x | x_n \le x < x_{n+1}\} = [x_n, x_{n+1})$ and the sequence of nodes, $\{x_n\}$, is increasing on the real line. The element is further discretized into $P+1$ distinct solution points $\boldsymbol{x}_n = [x_{n,1}, x_{n,2}, \ldots, x_{n,P+1}]^T$ where P is the degree of the piecewise interpolating polynomial representing the numerical solution in a given element. To reduce complexity, a uniform element size of $h = x_{n+1} - x_n, \forall n$ is used. A linear isoparametric mapping is introduced from the physical domain $x \in \Omega_n$ to the parent domain $\xi \in [-1, 1)$ such that

$$\xi|_{\Omega_n}(x) = 2(x - x_n) - 1, \qquad x \in [x_n, x_{n+1}). \tag{3}$$

The distribution of solution points across all elements in the parent domain is kept the same, $\boldsymbol{\xi} = (\xi_p)_{p=1,2,\ldots,P+1}$, so that the numerical solution in the nth element can be represented as

$$u_n^\delta(\xi, t) = \sum_{p=1}^{P+1} u_{n,p}^\delta(t)\ell_p(\xi), \qquad \xi \in [-1, 1), \tag{4}$$

where ℓ_p is the pth Lagrange polynomial.

Assuming exact time integration, Eq. (2) leads to a purely element-local description of the semi-discrete numerical equation,

$$\begin{aligned} &\frac{d\boldsymbol{u}^\delta{}_n}{dt} + 2a\boldsymbol{Q^1}(k)\boldsymbol{u}^\delta{}_n = 4\boldsymbol{Q^2}(k)\boldsymbol{u}^\delta{}_n, \qquad \forall n, \qquad t > 0, \\ &u^\delta{}_n(0) = \exp(ikx_n)\boldsymbol{w}_0(k), \end{aligned} \tag{5}$$

where $\boldsymbol{u}_n^\delta(t) = (u_{n,p}^\delta(t))_{p=1,2,\ldots,P+1}$ denotes the vector of solution values, $\boldsymbol{w}_0(k)$ is the collocation projection of the initial condition onto the solution points,

$$\boldsymbol{w}_0(k) = \left(\exp\left(ik\frac{1}{2}(1 + \xi_p)\right)\right)_{p=1,2,\ldots,P+1}, \tag{6}$$

and $\boldsymbol{Q^1}(k) \in \mathbb{C}^{(P+1)\times(P+1)}$ and $\boldsymbol{Q^2}(k) \in \mathbb{C}^{(P+1)\times(P+1)}$ are the first order and second order numerical differentiation operators in parent space. The definition of these operators depend on the numerical scheme being used and the constants 2 and 4 come from the transformation of the numerical differentiation operator from parent to physical space.

2.2. The Flux Reconstruction method

Under the Flux Reconstruction method, the first order numerical differentiation operator can be obtained by first defining a globally continuous, piecewise numerical solution polynomial of degree $P+1$ using correction function polynomials that convey boundary information to the interior of the element [6]. The numerical derivative is then obtained by differentiating this globally continuous solution,

$$\begin{aligned} a\frac{\delta u_n^\delta}{\delta x}(\xi, t) = 2\Bigg[&a\frac{\partial u_n^\delta}{\partial \xi}(\xi, t) + \left(au_L^\delta - au_n^\delta(-1, t)\right)\frac{dg_L}{d\xi}(\xi) \\ &+ \left(au_R^\delta - au_n^\delta(+1, t)\right)\frac{dg_R}{d\xi}(\xi)\Bigg], \qquad \xi \in [-1, 1), \end{aligned} \tag{7}$$

where $g_L(\xi), g_R(\xi) \in \mathbb{P}_{P+1}$ are the left-boundary and right-boundary correction functions in the parent space which satisfy the constraints,

$$\begin{aligned} &g_L(-1) = g_R(+1) = 1, \\ &g_L(+1) = g_R(-1) = 0, \end{aligned} \tag{8}$$

and can recover nodal DG, SD and various other high-order formulations [6,8]. The common interface fluxes, au_L^δ and au_R^δ, are computed from the polynomial functions on either side of the interface,

$$\begin{aligned} u_L^\delta &= (1 - \alpha)u_{n-1}^\delta(+1, t) + \alpha u_n^\delta(-1, t), \\ u_R^\delta &= (1 - \alpha)u_n^\delta(+1, t) + \alpha u_{n+1}^\delta(-1, t), \end{aligned} \tag{9}$$

where the upwinding coefficient, α, determines the type of common interface value used. A one-sided, upwinding flux is obtained

for $\alpha = 0.0$ and a centered flux is obtained for $\alpha = 0.5$. Eqs. (7) and (9) are now utilized to construct the numerical derivative,

$$\frac{\delta u_n^\delta}{\delta x}(\xi,t) = 2\left[\frac{\partial u_n^\delta}{\partial \xi}(\xi,t) + (1-\alpha)\left(u_{n-1}^\delta(+1,t) - u_n^\delta(-1,t)\right)\frac{dg_L}{d\xi}(\xi) + \alpha\left(u_{n+1}^\delta(-1,t) - u_n^\delta(+1,t)\right)\frac{dg_R}{d\xi}(\xi)\right], \quad \xi \in [-1,1). \tag{10}$$

This can then be transformed to a matrix-vector operation on $\boldsymbol{u}^\delta{}_n$,

$$\left.\frac{\delta \boldsymbol{u}^\delta}{\delta x}\right|_n = \sum_{j=-1}^{1} \boldsymbol{C_j} \boldsymbol{u}^\delta_{\boldsymbol{n+j}}, \tag{11}$$

where $\boldsymbol{C_j} \in \mathbb{R}^{(P+1)\times(P+1)}$ is given by

$$\boldsymbol{C_{-1}} = (1-\alpha)\boldsymbol{g_{L,\xi}}\ell_+^T,$$
$$\boldsymbol{C_0} = \boldsymbol{D} - (1-\alpha)\boldsymbol{g_{L,\xi}}\ell_-^T - \alpha\boldsymbol{g_{R,\xi}}\ell_+^T,$$
$$\boldsymbol{C_{+1}} = \alpha\boldsymbol{g_{R,\xi}}\ell_-^T.$$

Here $\boldsymbol{D} \in \mathbb{R}^{(P+1)\times(P+1)}$ is the polynomial differentiation operator such that

$$D_{p,m} = \frac{\mathrm{d}\ell_m}{\mathrm{d}\xi}(\xi_p), \qquad p,m = 1,2,\ldots,P+1, \tag{12}$$

where ℓ_m is the mth Lagrange polynomial in the parent domain. $\boldsymbol{g_{L,\xi}}, \boldsymbol{g_{R,\xi}} \in \mathbb{R}^{(P+1)\times 1}$ are the derivatives of the left-boundary and right-boundary correction functions at the solution points, and $\boldsymbol{\ell_-}, \boldsymbol{\ell_+} \in \mathbb{R}^{(P+1)\times 1}$ are the extrapolated values of the $P+1$ Lagrange basis polynomials,

$$\ell_{+_p} = \ell_p(+1), \qquad \ell_{-_p} = \ell_p(-1), \qquad p = 1,2,\ldots,P+1. \tag{13}$$

The second numerical derivative can be constructed by performing the same operation on the first numerical derivative. Let $\boldsymbol{v}_n^\delta = \left.\frac{\delta \boldsymbol{u}^\delta}{\delta x}\right|_n$, then,

$$\left.\frac{\delta^2 \boldsymbol{u}^\delta}{\delta x^2}\right|_n = \left.\frac{\delta \boldsymbol{v}^\delta}{\delta x}\right|_n = \sum_{j=-1}^{1} \boldsymbol{C_j} \boldsymbol{v}^\delta_{\boldsymbol{n+j}}. \tag{14}$$

The sinusoidal form of the initial condition in Eq. (5) provides the displacement relations, $\boldsymbol{u}^\delta_{\boldsymbol{n-1}} = \exp(-ik)\boldsymbol{u}^\delta_{\boldsymbol{n}}$, $\boldsymbol{u}^\delta_{\boldsymbol{n+1}} = \exp(ik)\boldsymbol{u}^\delta_{\boldsymbol{n}}$, which can then be used to obtain the numerical differentiation operators,

$$\boldsymbol{Q^1}(k) = \sum_{j=-1}^{1} \boldsymbol{C_j^{(1,1)}} \exp(ikj),$$
$$\boldsymbol{Q^2}(k) = \sum_{j=-2}^{2} \boldsymbol{B_j} \exp(ikj), \tag{15}$$

where $\boldsymbol{B_j} \in \mathbb{R}^{(P+1)\times(P+1)}$ is given by

$$\boldsymbol{B_{-2}} = \boldsymbol{C_{-1}^{(2,2)}}\boldsymbol{C_{-1}^{(2,1)}},$$
$$B_{-1} = \boldsymbol{C_{-1}^{(2,2)}}\boldsymbol{C_0^{(2,1)}} + \boldsymbol{C_0^{(2,2)}}\boldsymbol{C_{-1}^{(2,1)}},$$
$$B_0 = \boldsymbol{C_{+1}^{(2,2)}}\boldsymbol{C_{-1}^{(2,1)}} + \boldsymbol{C_0^{(2,2)}}\boldsymbol{C_0^{(2,1)}} + \boldsymbol{C_{-1}^{(2,2)}}\boldsymbol{C_{+1}^{(2,1)}},$$
$$B_{+1} = \boldsymbol{C_{+1}^{(2,2)}}\boldsymbol{C_0^{(2,1)}} + \boldsymbol{C_0^{(2,2)}}\boldsymbol{C_{+1}^{(2,1)}},$$
$$B_{+2} = \boldsymbol{C_{+1}^{(2,2)}}\boldsymbol{C_{+1}^{(2,1)}}.$$

Here (1, 1), (2, 1) and (2, 2) are identifiers used to differentiate between different correction procedures in the advection and diffusion terms. The first index in the superscript refers to the first or second order numerical differentiation operator while the second index refers to the correction procedure for the discontinuous solution or the discontinuous first derivative. The identifier defines the upwinding coefficient and correction functions used during the correction procedure, for example,

$$\boldsymbol{C_{+1}^{(1,1)}} = \alpha^{(1,1)}\boldsymbol{g_{R,\xi}^{(1,1)}}\boldsymbol{\ell}_-^T,$$
$$\boldsymbol{C_{+1}^{(2,1)}} = \alpha^{(2,1)}\boldsymbol{g_{R,\xi}^{(2,1)}}\boldsymbol{\ell}_-^T,$$
$$\boldsymbol{C_{+1}^{(2,2)}} = \alpha^{(2,2)}\boldsymbol{g_{R,\xi}^{(2,2)}}\boldsymbol{\ell}_-^T.$$

2.3. Analytical solution of the semi-discrete and exact equations

The analytical solution to the semi-discrete numerical equation, Eq. (5), can be found by exactly integrating the linear dynamical system in time using matrix factorization. The semi-discrete numerical equation can be rewritten as

$$\frac{d\boldsymbol{u}_n^\delta}{dt} + \boldsymbol{R}(a,k)\boldsymbol{u}_n^\delta = 0, \qquad \forall n, \qquad t > 0, \tag{16}$$

where $\boldsymbol{R}(a,k) \in \mathbb{C}^{(P+1)\times(P+1)}$ and,

$$\boldsymbol{R}(a,k) = 2a\,\boldsymbol{Q^1}(k) - 4\,\boldsymbol{Q^2}(k). \tag{17}$$

Assuming $\boldsymbol{R}(a,k)$ is diagonalizable,

$$\boldsymbol{R}(a,k) = \boldsymbol{W}(a,k)\boldsymbol{\Gamma}(a,k)\boldsymbol{W}^{-1}(a,k), \tag{18}$$

where $\boldsymbol{\Gamma}$ is the diagonal matrix of eigenvalues $\gamma_p(a,k) \in \mathbb{C}$ for $p = 1,2,\ldots,P+1$ and $\boldsymbol{W} \in \mathbb{C}^{P+1\times P+1}$ is the dense matrix containing eigenvectors of the differentiation operator. The initial condition can also be expanded in the basis of the eigenvectors,

$$\boldsymbol{w}_0(k) = \boldsymbol{W}(a,k)\boldsymbol{\beta}(a,k), \tag{19}$$

where $\beta_p(a,k) \in \mathbb{C}$ is the expansion coefficient along the pth column of $\boldsymbol{W}$, $\boldsymbol{w}_p(a,k)$, for $p = 1,2,\ldots,P+1$. The solution to Eq. (5) can now be written as

$$\begin{aligned}\boldsymbol{u}^\delta{}_n(t) &= \exp(-t\boldsymbol{R})\boldsymbol{u}^\delta{}_n(0)\\ &= \boldsymbol{W}\exp(-t\boldsymbol{\Gamma})\boldsymbol{W}^{-1}\exp(ikx_n)\boldsymbol{W}\boldsymbol{\beta}\\ &= \exp(ikx_n)\boldsymbol{W}\exp(-t\boldsymbol{\Gamma})\boldsymbol{\beta}\\ &= \exp(ikx_n)\sum_{p=1}^{P+1}\exp(-\gamma_p t)\beta_p\boldsymbol{w}_p.\end{aligned} \tag{20}$$

This shows that the numerical solution is a superposition of $P+1$ eigenmodes along the eigenvectors of $\boldsymbol{R}$ weighted by the expansion coefficients, β_p, of the initial condition. The time evolution of these modes is dictated by the eigenvalues γ_p.

The analytical solution to the exact equation, Eq. (2), on the vector of solution points $\boldsymbol{x}_n = x_n + \frac{1}{2}(1+\boldsymbol{\xi})$ can be found by sampling the functional form $\exp(ikx)\exp(-(aik+k^2)t)$,

$$\boldsymbol{u}_n(t) = \exp(ikx_n)\exp(-(aik+k^2)t)\sum_{p=1}^{P+1}\beta_p\boldsymbol{w}_p, \tag{21}$$

2.4. Stability, dissipation, dispersion and modal weights

The stability, dissipation and dispersion properties of the numerical scheme can be determined directly from the eigenvalues and eigenvectors of $\boldsymbol{R}$. The condition for numerical stability can be written as

$$\gamma_p^{\mathrm{Re}}(a,k) \geq 0 \text{ for } p = 1,2,\ldots,P+1, \tag{22}$$

which must hold for $k \in [0,(P+1)\pi]$ where the upper bound corresponds to the Nyquist limit for the mesh. The criteria for numerical dissipation and dispersion can be determined from the

Table 1
Upwinding coefficients and common names for DG schemes with different interface flux formulations.

Scheme	$\alpha^{(1,1)}$	$\alpha^{(2,1)}$	$\alpha^{(2,2)}$	Common name for DG scheme
Centered-centered	0.5	0.5	0.5	Centered advection - BR1 diffusion
Upwind-centered	0.0	0.5	0.5	Upwinded advection - BR1 diffusion
Centered-one-sided	0.5	1.0	0.0	Centered advection - LDG diffusion
Upwind-one-sided	0.0	1.0	0.0	Upwinded advection - LDG diffusion

equation for absolute error of the numerical solution,

$$\boldsymbol{e}_n(t) = \boldsymbol{u}^{\delta}{}_n(t) - \boldsymbol{u}_n(t) = \exp(ikx_n)\exp\left(-\left(aik+k^2\right)t\right) \times \sum_{p=1}^{P+1}\left[\exp\left(-\left(\gamma_p-\left(aik+k^2\right)\right)t\right)-1\right]\beta_p\boldsymbol{w}_p. \tag{23}$$

For the initial condition of an isolated Fourier component, each eigenmode contributes a certain amount of numerical dissipation and dispersion to the numerical solution. The numerical dissipation in an eigenmode is characterized by $\gamma_p^{\mathrm{Re}}(a,k) - k^2 > 0$ and leads to a mode which decays in amplitude more rapidly than the prescribed decay rate of physical diffusion. An eigenmode can also exhibit numerical anti-dissipation if $0 \le \gamma_p^{\mathrm{Re}}(a,k) < k^2$. In this case, the mode decays in amplitude at a slower rate. Numerical dispersion is present in an eigenmode if $\gamma_p^{\mathrm{Im}}(a,k) - ak \neq 0$. This causes the mode to propagate at an incorrect speed.

Since all $P+1$ eigenmodes are present in the numerical solution, it's important to determine how each mode contributes quantitatively through the modal weights, β_p. This quantity can best be described as a distribution of energy among all eigenmodes [21,22] and is important in determining whether the solution will decay or propagate at an incorrect speed.

2.5. Dissipation and dispersion error of nodal DG for advection-diffusion

The FR formulation can be used to recover various high-order schemes. In this study, we will focus our analysis on the nodal DG scheme on Gauss–Legendre points with different interface flux formulations. Table 1 defines the set of upwinding coefficients used to obtain common interface values for four different types of interface flux formulations. Since the nodal DG correction functions are used, the flux formulations for diffusion are able to recover two common schemes within the DG community: BR1 introduced by Bassi and Rebay [23] and local Discontinuous Galerkin (LDG) introduced by Cockburn and Shu [24]. For simplicity, the penalty term often used to stabilize the schemes [3] will be omitted so that LDG becomes minimal dissipation LDG [25].

The numerical dissipation and dispersion properties for the solution of advection-diffusion problems is dependent on the non-dimensional parameter a. For most results in this paper, a non-dimensional parameter of $a = 10$ is chosen for illustration. Figs. 1–3 show the dissipation, dispersion and modal weight of each eigenmode for a centered-centered and upwind-one-sided schemes of polynomial order, $P = 2$. We see that for one of the modes, designated mode 1, the dissipation and dispersion errors vanish in the asymptotic limit of $k \to 0$, and the squared modal weight $|\beta_1|^2 \to P+1$. This mode is defined as the physical mode and its existence and uniqueness have been proven for advection problems [22]. Regarding the effect of interface fluxes, we see that both schemes have little dispersion or dissipation for low wavenumbers. For higher wavenumbers, the physical mode of the upwind-one-sided scheme remains dominant and the scheme is more dissipative. On the other hand, the physical mode of the centered-centered scheme loses its dominance as can be seen from Fig. 3. Moreover, close to the Nyquist limit, all the modes for this scheme are anti-dissipative.

Even though the chosen flux is a linear function of the state, the state itself is sinusoidal and cannot be expressed in any finite-dimensional polynomial basis. Correspondingly, the location of solution points has a direct impact on the distribution of the initial condition among the $P+1$ eigenmodes. This can be observed from Fig. 4 which plots the distribution of energy among the 3 eigenmodes for the centered-centered DG scheme with $P = 2$, advection-diffusion parameter $a = 10$, using Gauss–Legendre, equidistant and Gauss–Lobatto points respectively.

3. Spectral comparison

This section provides an investigation into the relative error generated by the nodal DG scheme with different interface flux formulations for the full range of resolvable wavenumbers. A resolving efficiency is defined in order to measure the fraction of resolved waves that propagate with minimal error. We see that the centered-centered scheme produces the least amount of relative error for a well resolved solution while the centered-one-sided scheme leads to the least amount of relative error for solutions that are under-resolved.

3.1. Relative error and resolving efficiency

A measure of relative error can be derived by using the vector ℓ^2 norm of absolute error. The use of a pointwise error is motivated by the nodal nature of the FR formulation and is different from the L^2 functional norm that measures integrated error over a fixed domain. Consider the vector ℓ^2 norm of the absolute error using Eq. (23),

$$\begin{aligned}\|\boldsymbol{e}_n(t)\|_{\ell^2} &= \|\boldsymbol{u}^{\delta}{}_n(t) - \boldsymbol{u}_n(t)\|_{\ell^2} \\ &= \exp(-k^2t)\left\|\sum_{p=1}^{P+1}\left[\exp\left(-\left(\gamma_p-\left(aik+k^2\right)\right)t\right)-1\right]\beta_p\boldsymbol{w}_p\right\|_{\ell^2},\end{aligned} \tag{24}$$

where we have used that $|\exp(\zeta)| = 1$ if ζ is purely imaginary. Similarly, the norm of the analytical solution to the exact equation, Eq. (21) is given by

$$\begin{aligned}\|\boldsymbol{u}_n(t)\|_{\ell^2} &= \exp\left(-k^2t\right)\|\boldsymbol{w}_0\|_{\ell^2}, \\ &= \exp\left(-k^2t\right)\sqrt{\sum_{p=1}^{P+1}\left|\exp\left(ik\frac{1}{2}(1+\xi_p)\right)\right|^2}, \\ &= \exp\left(-k^2t\right)\sqrt{P+1}.\end{aligned} \tag{25}$$

A relative error can then be defined by taking the difference between Eqs. (24) and (25),

$$\frac{\|\boldsymbol{e}_n(t)\|_{\ell^2}}{\|\boldsymbol{u}_n(t)\|_{\ell^2}} = \frac{1}{\sqrt{P+1}}\left\|\sum_{p=1}^{P+1}\left[\exp(-(\gamma_p-(aik+k^2))t)-1\right]\beta_p\boldsymbol{w}_p\right\|_{\ell^2}. \tag{26}$$

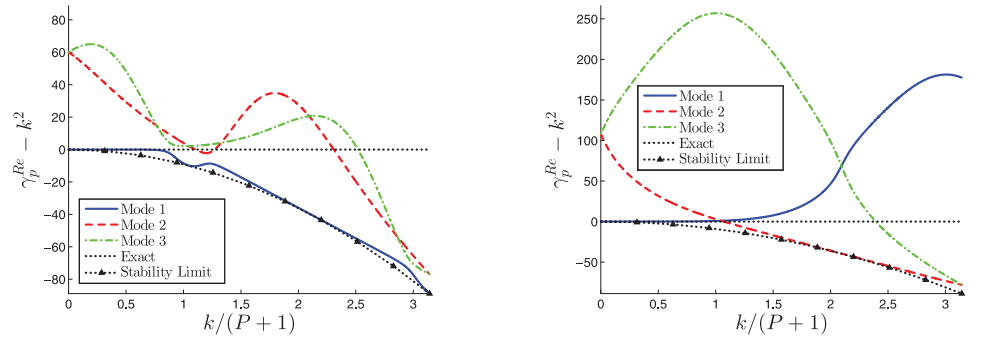

(a) Centered-centered scheme: $\alpha^{(1,1)} = 0.5,\ \alpha^{(2,1)} = 0.5,\ \alpha^{(2,2)} = 0.5$

(b) Upwind-one-sided scheme: $\alpha^{(1,1)} = 0.0,\ \alpha^{(2,1)} = 1.0,\ \alpha^{(2,2)} = 0.0$

Fig. 1. Numerical dissipation in each eigenmode $p = 1, 2, 3$ for the DG scheme of order $P = 2$ using Gauss–Legendre solution points solving the advection-diffusion equation, $a = 10$.

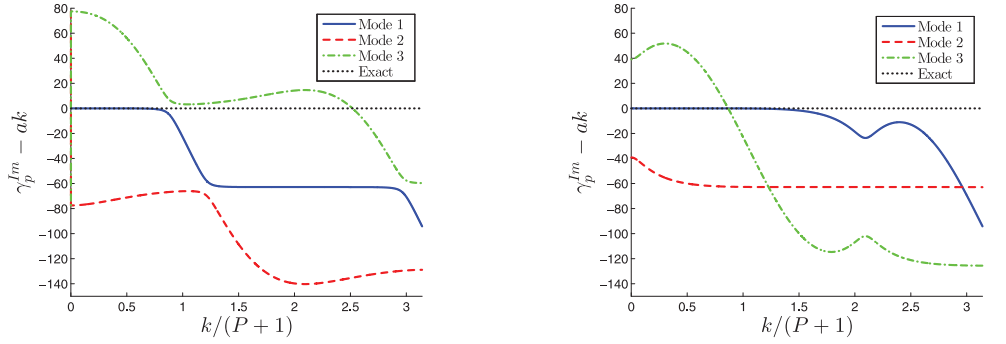

(a) Centered-centered scheme: $\alpha^{(1,1)} = 0.5,\ \alpha^{(2,1)} = 0.5,\ \alpha^{(2,2)} = 0.5$

(b) Upwind-one-sided scheme: $\alpha^{(1,1)} = 0.0,\ \alpha^{(2,1)} = 1.0,\ \alpha^{(2,2)} = 0.0$

Fig. 2. Numerical dispersion in each eigenmode $p = 1, 2, 3$ for the DG scheme of order $P = 2$ using Gauss–Legendre solution points solving the advection-diffusion equation, $a = 10$.

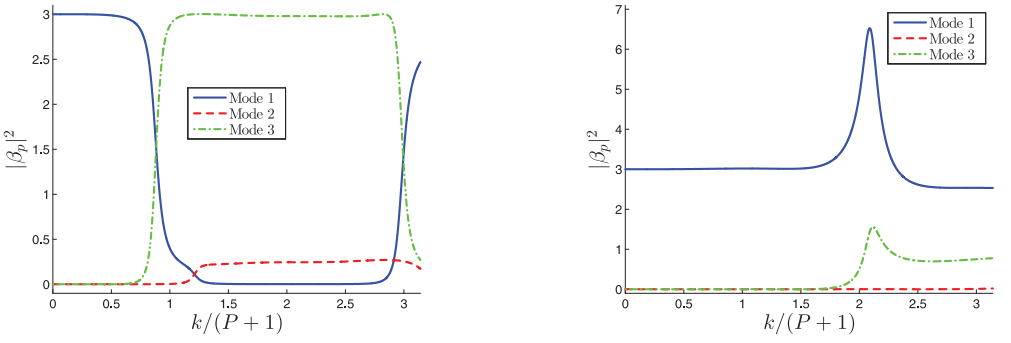

(a) Centered-centered scheme: $\alpha^{(1,1)} = 0.5,\ \alpha^{(2,1)} = 0.5,\ \alpha^{(2,2)} = 0.5$

(b) Upwind-one-sided scheme: $\alpha^{(1,1)} = 0.0,\ \alpha^{(2,1)} = 1.0,\ \alpha^{(2,2)} = 0.0$

Fig. 3. Energy distributed among each eigenmode $p = 1, 2, 3$ for the DG scheme of order $P = 2$ using Gauss–Legendre solution points solving the advection-diffusion equation, $a = 10$.

The triangle inequality can be used to eliminate the dependency on the eigenvectors,

$$\frac{\|\boldsymbol{e}_n(t)\|_{\ell^2}}{\|\boldsymbol{u}_n(t)\|_{\ell^2}} \leq \frac{1}{\sqrt{P+1}} \sum_{p=1}^{P+1} \|\left[\exp\left(-\left(\gamma_p - \left(aik + k^2\right)\right)t\right) - 1\right]\beta_p \boldsymbol{w}_p\|_{\ell^2},$$
$$= \frac{1}{\sqrt{P+1}} \sum_{p=1}^{P+1} \left|\exp\left(-\left(\gamma_p - \left(aik + k^2\right)\right)t\right) - 1\right| |\beta_p|. \tag{27}$$

Then in the limit of $t \to 0$,

$$\lim_{t\to 0} \frac{\|\boldsymbol{e}_n(t)\|_{\ell^2}}{\|\boldsymbol{u}_n(t)\|_{\ell^2}} \leq \frac{1}{\sqrt{P+1}} \sum_{p=1}^{P+1} \left|\gamma_p - (aik + k^2)\right| |\beta_p|\, t + \mathcal{O}(t^2), \tag{28}$$

which gives an upper bound on the initial relative error. In other words, the initial slope of the relative error can be written as

$$\lim_{t\to 0} \frac{1}{t} \frac{\|\boldsymbol{e}_n(t)\|_{\ell^2}}{\|\boldsymbol{u}_n(t)\|_{\ell^2}} \leq \frac{1}{\sqrt{P+1}} \sum_{p=1}^{P+1} \left|\gamma_p - (aik + k^2)\right| |\beta_p| = \phi(a, k), \tag{29}$$

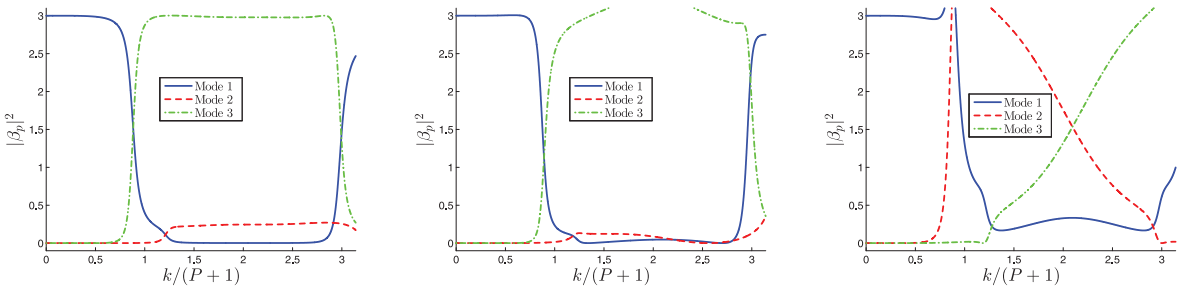

(a) Gauss-Legendre (b) Equidistant (c) Gauss-Lobatto

Fig. 4. Energy distributed among each eigenmode $p = 1, 2, 3$ for the centered-centered, DG scheme of order $P = 2$ solving the advection-diffusion equation, $a = 10$.

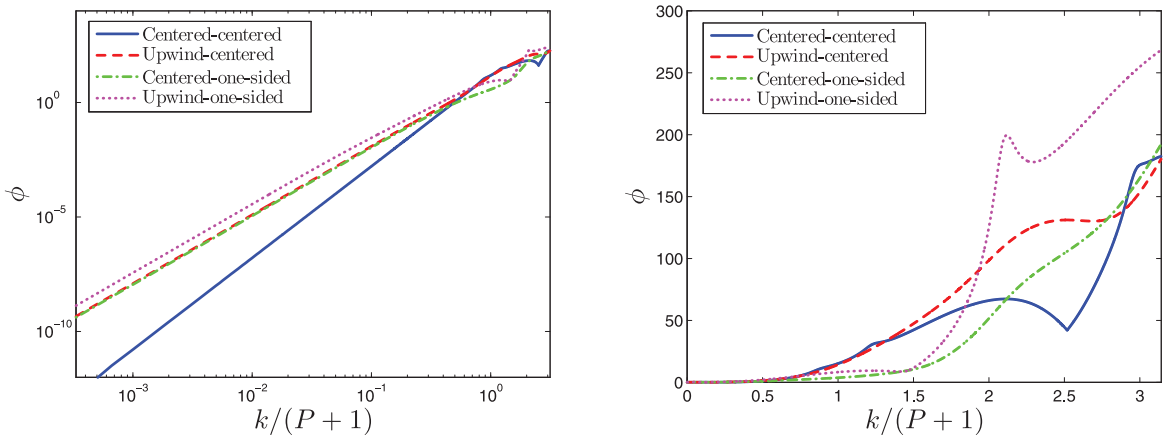

(a) Log Scale (b) Linear Scale

Fig. 5. Upper bound on initial slope of the relative error vs. nondimensional wavenumber for the DG scheme of order $P = 2$ using Gauss–Legendre solution points solving the advection-diffusion equation, $a = 10$.

which shows that the initial growth of error is determined by the products of eigenvalue errors and modal weights of the system. Based on [21,26], a resolving efficiency can now be defined as

$$\eta = \frac{k_f}{(P+1)\pi}, \tag{30}$$

where k_f is such that

$$\phi(a, k) \leq \epsilon \qquad \text{for} \qquad k \leq k_f. \tag{31}$$

η measures the fraction of resolved waves that are propagated with minimal error. The initial growth rate of error for these waves are guaranteed to be less than the specified slope tolerance, ϵ.

3.2. Spectral comparison of nodal DG with different interface fluxes

Fig. 5 plots the initial slope of the relative error, Eq. (29), for the four types of interface flux formulations in Table 1 for an advection-diffusion problem with $a = 10$. We see that for low wavenumbers or well resolved waves, the centered-centered scheme produces the least amount of error. For larger wavenumbers up to $k/(P+1) \approx 2$, the centered-one-sided scheme generates the least amount of error.

Table 2 lists the resolving efficiencies for different interface flux formulations and polynomial orders. A slope tolerance of $\epsilon = 0.1$ is used to compare the ability of a scheme to capture well resolved waves. We see that the centered-centered scheme produces a better resolving efficiency for even or high polynomial orders while the centered-one-sided scheme produces a higher resolving efficiency for odd polynomials of low order. Interestingly, the commonly used upwind-one-sided scheme is not the best for any polynomial order.

4. Time integration and CFL restriction

This section discusses the CFL restriction of nodal DG with different interface flux formulations for the advection, diffusion and advection-diffusion equations on tensor product elements. Towards this end, the fully discrete advection-diffusion equation is constructed for a general explicit, M-stage Runge–Kutta (RK) type scheme and the stability criterion is imposed to solve for the maximum nondimensional time step of the discrete linear dynamical system. We show that the minimum of the maximum stable time steps for pure-advection and pure-diffusion is inadequate when choosing a maximum stable time step for the advection-diffusion equation. However, a conservative prediction can be obtained from the harmonic sum of the maximum stable time steps for the advection and diffusion equations. We propose extensions to multidimensional tensor product elements in structured as well as unstructured grids and to the Navier–Stokes equations. Along the way, we also show that the centered-centered scheme has the least restrictive CFL with a limit around 5 times larger than the CFL limit for the upwind-one-sided scheme for certain wavenumbers.

4.1. Multi-stage explicit time integration scheme

The fully discrete numerical update equation can be obtained from Eq. (16)

$$\frac{\delta \boldsymbol{u}_n^\delta}{\delta t} = -\boldsymbol{R}(a, k)\boldsymbol{u}_n^\delta, \qquad \forall n, \qquad t > 0. \tag{32}$$

Table 2
Resolving efficiencies, $\epsilon = 0.1$, for the DG scheme using Gauss–Legendre solution points solving the advection-diffusion equation, $a = 10$.

P	Centered-centered	Upwind-centered	Centered-one-sided	Upwind-one-sided
1	0.0296	0.0297	0.0469	0.0464
2	0.0887	0.0650	0.0684	0.0507
3	0.0872	0.0842	0.0932	0.0884
4	0.1145	0.1120	0.1091	0.1034
5	0.1482	0.1350	0.1245	0.1211

In the case of a general explicit, M-stage Runge–Kutta (RK) time integration scheme, the numerical solution can be written as

$$\boldsymbol{u}_{\boldsymbol{n}}^{\delta}(t+\Delta t) = \boldsymbol{S}(a,k,\Delta t)\boldsymbol{u}_{\boldsymbol{n}}^{\delta}(t), \qquad \forall n, \qquad t > 0, \tag{33}$$

where Δt is the numerical time step and $\boldsymbol{S}(a, k, \Delta t)$ is the numerical integration operator,

$$\boldsymbol{S}(a,k,\Delta t) = \sum_{m=0}^{M} (-1)^m \frac{\nu_m}{m!} \Delta t^m \boldsymbol{R}(a,k)^m, \tag{34}$$

where ν_m for $m = 0, 1, \ldots, M$ are coefficients of the RK scheme and M is the number of stages.

4.2. Stability criteria

The stability criteria of the discrete linear dynamical system in Eq. (33) can be written as

$$\rho(\boldsymbol{S}(a,k,\Delta t)) \leq 1 \qquad \forall k \in [0, (P+1)\pi], \tag{35}$$

where ρ is the spectral radius. The computation of the spectral radius requires the eigenvalues of $\boldsymbol{S}(a, k, \Delta t)$ which can be found by using the eigendecomposition from Eq. (18) as

$$\begin{aligned} \boldsymbol{S}(a,k,\Delta t) &= \boldsymbol{W}(a,k)\left[\sum_{m=0}^{M} (-1)^m \frac{\nu_m}{m!} \Delta t^m \boldsymbol{\Gamma}(a,k)^m\right] \boldsymbol{W}^{-1}(a,k), \\ &= \boldsymbol{W}(a,k)\boldsymbol{\Lambda}(a,k,\Delta t)\boldsymbol{W}^{-1}(a,k) \end{aligned} \tag{36}$$

where $\boldsymbol{\Lambda}$ is the diagonal matrix of eigenvalues $\lambda_p(a, k, \Delta t) \in \mathbb{C}$ for $p = 1, 2, \ldots, P+1$. The maximum time step can then be obtained as the solution to

$$\begin{aligned} &\text{maximize} \quad \Delta t \\ &\text{subject to} \quad \max_{p=1}^{P+1} |\lambda_p(a,k,\Delta t)| \leq 1, \qquad \forall k \in [0, (P+1)\pi], \end{aligned} \tag{37}$$

for a given time integration scheme and nondimensional wavespeed a. To find the stability criteria, the nondimensional timestep is transformed back into a physical time step using the transformation introduced in the beginning of Section 2,

$$\Delta \hat{t} \leq \Delta \hat{t}_{max} = \Delta t_{max} \frac{h^2}{\hat{b}}. \tag{38}$$

In the subsections to follow, we use a standard 4 stage, 4th order Runge–Kutta (RK44) scheme for illustration. A bisection method is used to find Δt_{max}.

4.3. CFL restrictions on advection-diffusion

The maximum physical time step, $\Delta \hat{t}_{max}$, is used to compare the CFL restrictions for all wavenumbers for advection, diffusion and advection-diffusion problems. Fig. 6 plots the maximum physical time step for different equations using $P = 2$ and $P = 3$. The figure shows that the coupling of advection and diffusion decreases the maximum physical time step for all wavenumbers leading to a stricter CFL limit. Hence, choosing the minimum of the maximum stable time steps for the advection equation and diffusion equation is inadequate when choosing a time step for the advection-diffusion equation.

Table 3
Maximum nondimensional time steps for the RK44, DG scheme using Gauss–Legendre points.

	Δt_{max}^{adv}		Δt_{max}^{diff}	
P	Centered	Upwind	Centered	One-sided
1	0.707	0.464	0.174	0.0773
2	0.349	0.235	0.0426	0.0187
3	0.213	0.145	0.0158	0.00634
4	0.143	0.100	0.00719	0.00266
5	0.103	0.0736	0.00373	0.00129

4.4. CFL restrictions of nodal DG with different interface fluxes

Fig. 7 plots the maximum nondimensional time step for the four types of interface flux formulations in Table 1 using $P = 2$ and $P = 3$ for an advection-diffusion problem with $a = 10$. We see that the centered-centered scheme has the least restrictive CFL limit while the upwind-one-sided scheme has the most restrictive CFL limit. In fact, the CFL limit of the centered-centered scheme is larger than the upwind-one-sided scheme for all wavenumbers and around 5 times larger for certain wavenumbers.

4.5. Conservative prediction method for $\Delta \hat{t}$

The stability criterion in Eq. (38) gives an exact value for the maximum physical time step for an advection-diffusion problem but requires the knowledge of a multi-variable, nonlinear function Δt_{max} which changes depending on the time integration scheme, choice of correction function, common interface value, polynomial order and non-dimensional parameter $a = \hat{a}h/\hat{b}$. Several prediction methods are often used in an effort to reduce the dependency of Δt_{max} on a with the hopes that the method is conservative. One method is to use the minimum of the maximum stable time steps for pure-advection and pure-diffusion,

$$\begin{aligned} \Delta \hat{t} &\leq \min\left(\Delta t_{\max}^{adv} \frac{h}{\hat{a}},\ \Delta t_{\max}^{diff} \frac{h^2}{\hat{b}}\right) \qquad \text{or} \\ \Delta t_{\max} &= \min\left(\Delta t_{\max}^{adv} \frac{1}{a},\ \Delta t_{\max}^{diff}\right), \end{aligned} \tag{39}$$

where Δt_{max}^{adv} and Δt_{max}^{diff} are the maximum nondimensional time steps for the advection and diffusion equations, respectively. These values can be determined by removing the diffusion or advection term in the fully discrete equation and solving the optimization problem in Eq. (37). Table 3 provides these values for a variety of common interface values and polynomial orders.

A more conservative method that is used for the Navier–Stokes equation [3,27,28] is the harmonic sum of the maximum stable time steps for the advection equation and the diffusion equation,

$$\Delta \hat{t} \leq \frac{1}{\frac{\hat{a}}{\Delta t_{max}^{adv} h} + \frac{\hat{b}}{\Delta t_{max}^{diff} h^2}} \qquad \text{or} \qquad \Delta t_{max} = \frac{1}{\frac{a}{\Delta t_{max}^{adv}} + \frac{1}{\Delta t_{max}^{diff}}}. \tag{40}$$

Fig. 8 shows how these methods compare with the exact maximum nondimensional time step for $P = 2$. The estimate in

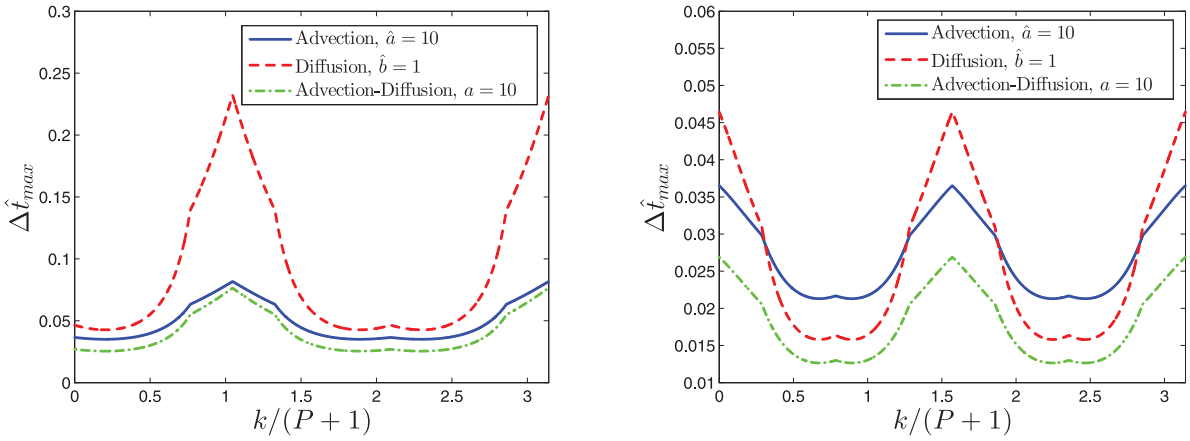

Fig. 6. Maximum physical time step, $\Delta \hat{t}_{max}$, vs. nondimensional wavenumber for the RK44, DG, centered-centered scheme using Gauss–Legendre solution points.

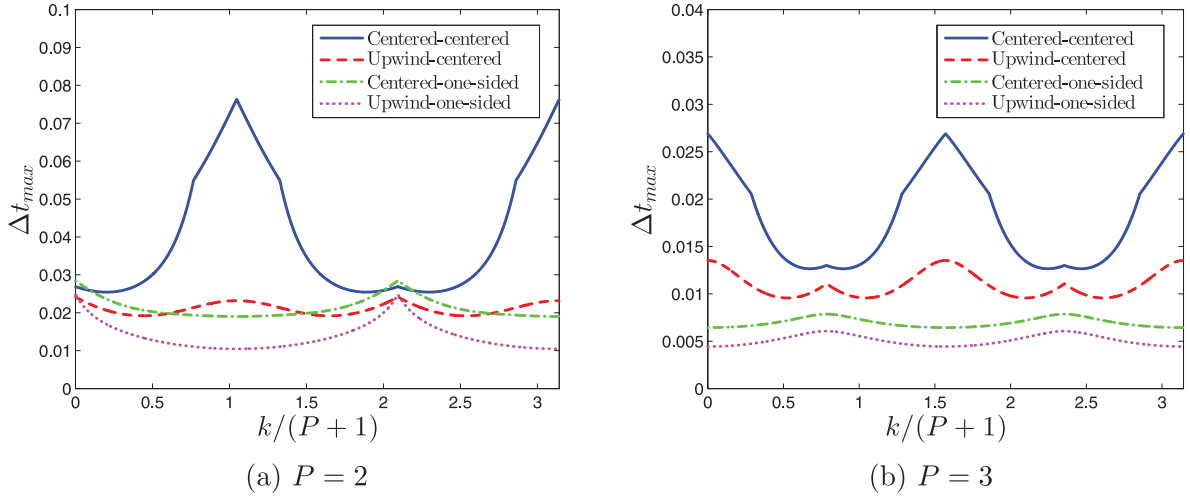

Fig. 7. Maximum nondimensional time step, Δt_{max}, vs. nondimensional wavenumber, $k/(P+1)$, for the RK44, DG scheme using Gauss–Legendre solution points solving the advection-diffusion equation, $a = 10$.

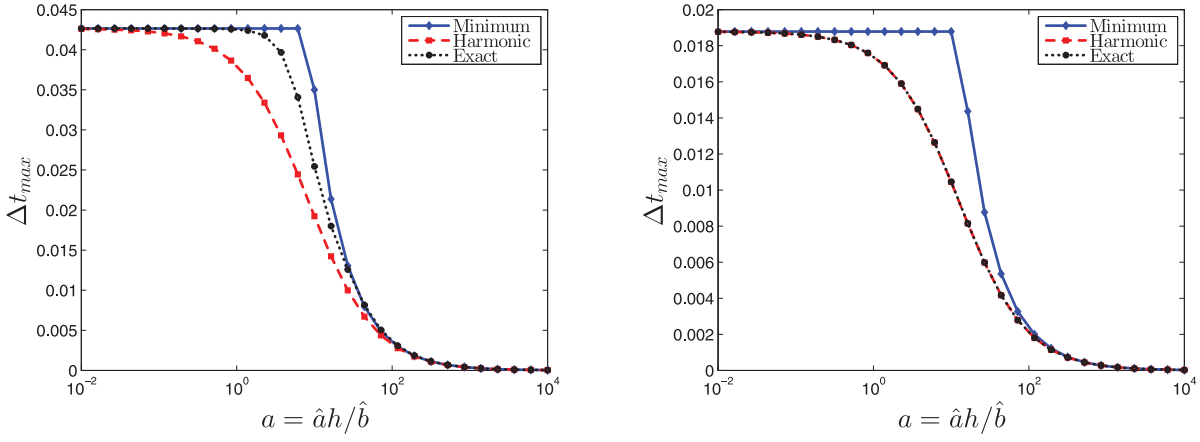

Fig. 8. Maximum nondimensional time step estimates vs. nondimensional wavespeed for the RK44, DG scheme of order $P = 2$ using Gauss–Legendre solution points.

Eq. (39) is at or above the maximum allowable timestep for all values of a clearly showing that it fails as a conservative prediction method. On the other hand, the harmonic sum gives conservative predictions for the full range of advection-diffusion problems. Moreover, in the case of the upwind-one-sided scheme, a prediction based on the harmonic sum almost exactly matches the exact CFL limit. These observations hold for other choices of common interface values and polynomial orders as well, showing that Eq. (40) can be used as a conservative estimate for the CFL restriction. Fig. 8 also shows that $a \approx 10$ is near a region where the coupling of advection and diffusion has a dramatic effect on the CFL limit of the scheme. In the case of the centered-centered scheme, the harmonic sum is still conservative but loses accuracy near $a \approx 10$.

4.6. Extension to tensor product elements

The 1D FR formulation for advection-diffusion can be extended to quadrilateral and hexahedral elements as discussed in [6,7,29]. This subsection proposes a method for extending the time step estimate from Eq. (40) to non-curved tensor product elements. For simplicity, the discussion focuses on rectilinear and quadrilateral meshes but the methodology can be easily extended to hexahedral elements.

Consider a multidimensional linear advection-diffusion problem,

$$\frac{\partial u}{\partial \hat{t}} + \sum_{d=1}^{N_d} \hat{a}_d \frac{\partial u}{\partial \hat{x}_d} = \hat{b} \sum_{d=1}^{N_d} \frac{\partial^2 u}{\partial \hat{x}_d^2}, \qquad \hat{x}_d \in \mathbb{R}, \qquad \hat{t} > 0,$$

where N_d is the number of spatial dimensions, $\hat{a}_d$ is the advection coefficient in the dth dimension and the domain is partitioned into N_{eles} non-overlapping, conforming tensor product elements, $\Omega = \bigcup_{n=1}^{N_{\text{eles}}} \Omega_n$.

In the special case of a rectangular element, the element domain is defined by $\Omega_n = \{[x_{d,n}, x_{d,n+1}) \text{ for } d = 1, 2, \ldots, N_d\}$. Each element is further discretized into $(P+1)^{N_d}$ distinct solution points where each point belongs to N_d sets of $P+1$ collinear points allowing for a simple extension of the one-dimensional case to multiple dimensions. The rectangular element size is defined by N_d side lengths of $h_d = x_{d,n+1} - x_{d,n}$ for $d = 1, 2, \ldots, N_d$ and a linear isoparametric mapping is again used on the physical domain. The fully discrete numerical equation can now be constructed by following the same procedure as before,

$$\frac{\delta \boldsymbol{u}_{\boldsymbol{n}}^{\delta}}{\delta t} = -\hat{\boldsymbol{R}} \boldsymbol{u}_{\boldsymbol{n}}^{\delta}, \qquad \forall n, \qquad t > 0. \tag{41}$$

where $\hat{\boldsymbol{R}}$ is defined as,

$$\hat{\boldsymbol{R}}\left(\hat{a}_1, \cdots, \hat{a}_{N_d}, \hat{b}, \hat{k}_1, \cdots, \hat{k}_{N_d}, h_1, \cdots, h_{N_d}\right) = \sum_{d=1}^{N_d} \left[\frac{2\hat{a}_d}{h_d} \mathbf{Q}_{\boldsymbol{d}}^{\boldsymbol{1}}\left(\hat{k}_d h_d\right) - \frac{4\hat{b}}{h_d^2} \mathbf{Q}_{\boldsymbol{d}}^{\boldsymbol{2}}\left(\hat{k}_d h_d\right) \right], \tag{42}$$

and the equation can again be integrated using a general explicit, M-stage RK scheme to produce a similar stability criteria as Eq. (35). The conservative prediction method for $\Delta\hat{t}$ from Eq. (40) can now be extended, in a similar manner, to estimate the time step of the problem,

$$\Delta\hat{t} \leq \frac{1}{\sum_{d=1}^{N_d} \left[\frac{\hat{a}_d}{\Delta t_{max}^{adv} h_d} + \frac{\hat{b}}{\Delta t_{max}^{diff} h_d^2} \right]}. \tag{43}$$

In the case of a non-rectangular element, we can construct a maximum time step estimate as the harmonic sum of estimates for each dimension. Each edge of the quadrilateral element contains $P+1$ distinct flux points for a total of $N_{\text{fpts}} = 4(P+1)$ flux points. A time step estimate on each flux point can be computed as,

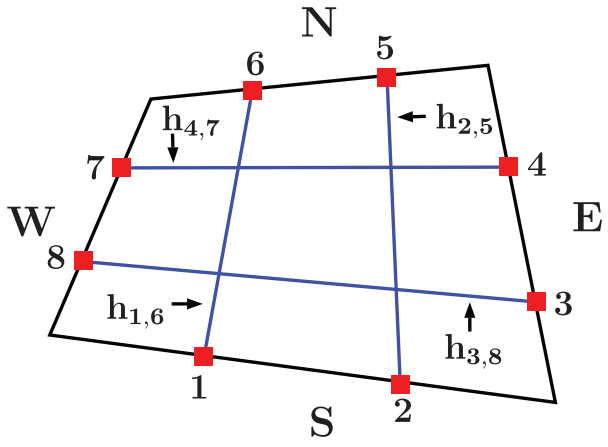

Fig. 9. A visual representation of a quadrilateral element for a polynomial order of $P = 1$. The flux points are marked by red squares and west, east, south and north faces are represented by *W, E, S, N*, respectively. The distances between flux points, $h_{1,6}$, $h_{3,8}$, $h_{2,5}$, $h_{4,7}$ are used to estimate the maximum time step in the element.

$$\Delta\hat{t}_m = \frac{\Delta t_{max}^{adv} h_m}{|\hat{a}_m|} + \frac{\Delta t_{max}^{diff} h_m^2}{\hat{b}} \qquad m = 1, 2, \ldots, N_{\text{fpts}}, \tag{44}$$

where $|\hat{a}_m|$ is the absolute value of the advection coefficient normal to the face and h_m are distances between flux points defined in Fig. 9, for example, $h_1 = h_6 = h_{1,6}$. The minimum time step is then computed on each face. From Fig. 9, the minimum time steps computed on the west, east, south and north faces are

$$\Delta\hat{t}^W = \min\left(\Delta\hat{t}_7, \Delta\hat{t}_8\right), \qquad \Delta\hat{t}^E = \min\left(\Delta\hat{t}_3, \Delta\hat{t}_4\right), \tag{45}$$

$$\Delta\hat{t}^S = \min\left(\Delta\hat{t}_1, \Delta\hat{t}_2\right), \qquad \Delta\hat{t}^N = \min\left(\Delta\hat{t}_5, \Delta\hat{t}_6\right). \tag{46}$$

Finally from Eq. (40), the maximum time step estimate can be based on a harmonic sum of the minimum time step for each dimension,

$$\Delta\hat{t} \leq \frac{1}{\frac{1}{\min\left(\Delta\hat{t}^W, \Delta\hat{t}^E\right)} + \frac{1}{\min\left(\Delta\hat{t}^S, \Delta\hat{t}^N\right)}}. \tag{47}$$

4.7. Extension to Navier–Stokes equations

Consider the unsteady, two-dimensional, compressible Navier–Stokes equations in conservative form,

$$\frac{\partial U}{\partial \hat{t}} + \frac{\partial F_{\text{inv}}}{\partial \hat{x}_1} + \frac{\partial G_{\text{inv}}}{\partial \hat{x}_2} = \frac{\partial F_{\text{visc}}}{\partial \hat{x}_1} + \frac{\partial G_{\text{visc}}}{\partial \hat{x}_2} \tag{48}$$

where,

$$U = \begin{pmatrix} \rho \\ \rho u \\ \rho v \\ e \end{pmatrix}, \quad F_{\text{inv}} = \begin{pmatrix} \rho u \\ \rho u^2 + p \\ \rho uv \\ (e+p)u \end{pmatrix}, \quad G_{\text{inv}} = \begin{pmatrix} \rho v \\ \rho vu \\ \rho v^2 + p \\ (e+p)v \end{pmatrix},$$

$$F_{\text{visc}} = \begin{pmatrix} 0 \\ \sigma_{11} \\ \sigma_{12} \\ u\sigma_{11} + v\sigma_{21} - q_1 \end{pmatrix}, \quad G_{\text{visc}} = \begin{pmatrix} 0 \\ \sigma_{21} \\ \sigma_{22} \\ u\sigma_{12} + v\sigma_{22} - q_2 \end{pmatrix}, \tag{49}$$

where ρ is density, u, v are the velocity components in the $\hat{x}_1, \hat{x}_2$ directions, respectively, and e is total energy per unit volume. The pressure is determined from the equation of state,

$$p = (\gamma - 1)\left(e - \frac{1}{2}\rho\left(u^2 + v^2\right)\right), \tag{50}$$

where γ is the ratio of specific heats. For a Newtonian fluid, the viscous stresses are

$$\sigma_{ij} = \mu\left(\frac{\partial u_i}{\partial \hat{x}_j} + \frac{\partial u_j}{\partial \hat{x}_i}\right) - \frac{2}{3}\mu\delta_{ij}\frac{\partial u_k}{\partial \hat{x}_k}, \tag{51}$$

and the heat fluxes are

$$q_i = -k\frac{\partial T}{\partial \hat{x}_i}, \tag{52}$$

where $k = C_p\mu/\mathrm{Pr}$, $T = p/(\rho R)$, Pr is the Prandtl number, C_p is the specific heat at constant pressure, R is the gas constant and μ is the dynamic viscosity.

As before, a time step estimate on each flux point can be computed as,

$$\Delta\hat{t}_m = \frac{\Delta t^{adv}_{max}\, h_m}{|\lambda_m|} + \frac{\Delta t^{diff}_{max}\, h_m^2}{\nu_m} \qquad m = 1, 2, \ldots, N_{\text{fpts}}, \tag{53}$$

where λ_m and ν_m are the numerical wavespeeds and numerical diffusion coefficients on each flux point, respectively. From [28], these can be estimated as,

$$|\lambda_m| = |V_m| + c_m, \quad \nu_m = \max\left(\frac{\mu_m}{\rho_m}, \frac{\gamma\mu_m}{\mathrm{Pr}\rho_m}\right), \quad m = 1, 2, \ldots, N_{\text{fpts}}, \tag{54}$$

where V_m is the velocity normal to the face and $c_m = \sqrt{\frac{\gamma p_m}{\rho_m}}$ is the speed of sound. The maximum time step can then be estimated from Eq. (47).

5. Numerical tests

In this section, we verify the results obtained in the previous sections by solving the advection-diffusion and Navier–Stokes equations on 1D uniform, 2D rectilinear and 2D unstructured grids. The numerical tests for advection-diffusion confirm that the centered-centered scheme generates the least amount of error for well resolved solutions while the centered-one-sided scheme generates the least amount of error for solutions that are under-resolved. For the Navier–Stokes equations, $P = 2$, the upwind-centered scheme generates the least amount of error for well resolved solutions while the upwind-one-sided scheme generates the least amount of error for solutions that are under-resolved. These results match the expectations in Section 3. The CFL restrictions established in Section 4 are also verified and the formula in Eq. (43) is shown to be an effective prediction for the maximum stable time step for both the advection-diffusion and Navier–Stokes equations on Cartesian grids. In the case of unstructured grids, this time step estimate is not always conservative but it is still fairly accurate.

In the numerical tests that follow, the correction functions and solution point locations are chosen to recover the nodal DG scheme on Gauss–Legendre points and a standard 4 stage, 4th order RK scheme is used for time integration.

5.1. Case 1: 1D advection-diffusion of an approximate Gaussian

The first test case involves the solution of the 1D advection-diffusion equation with an initial condition of an approximate Gaussian and periodic boundary conditions. The domain is chosen as $\hat{x} \in [-10, 10]$ and $N_{\text{eles}} = 20$ elements are used to construct a uniform mesh with $h = 1$. An advection speed of $\hat{a} = 10$ and a diffusion coefficient of $\hat{b} = 1$ are used in order to test cases with a nondimensional wavespeed of $a = 10$. All cases have been verified to be stable using the maximum stable time step estimate proposed in Eq. (40). We choose to use half of this estimate to minimize time integration errors.

The initial condition and exact solution of an approximate Gaussian can be computed from,

$$u_{n,p}(\hat{t}) = \sum_{j=-N_{\hat{k}}}^{N_{\hat{k}}} \theta_j \exp\left(-\hat{b}\hat{k}_j^2\hat{t}\right)\cos\left(\hat{k}_j\left(\hat{x}_{n,p} - \hat{a}\hat{t}\right)\right), \tag{55}$$

where θ_j is the jth spectral weight, $\hat{k}_j = 2\pi j/L$ is the jth wavenumber associated with the domain length, $L = 20$, and $N_{\hat{k}}$ is the number of waves used. $N_{\hat{k}}$ is chosen to be the largest value under the constraint $\hat{k}_{N_{\hat{k}}} \leq (P+1)\pi/h$. The spectral weights are defined as

$$\theta_j = \frac{\exp(-(\sigma\hat{k}_j)^2/2)}{\sqrt{2\pi}\sigma\sum_{s=-N_{\hat{k}}}^{N_{\hat{k}}}\exp(-(\sigma\hat{k}_s)^2/2)}, \qquad -N_{\hat{k}} \leq j \leq N_{\hat{k}}, \tag{56}$$

where σ is the standard deviation of the Gaussian. The standard deviation dictates the width of the Gaussian and changes the spectral weight distribution across the wave spectrum.

The vector ℓ^2 norm of the relative error is computed as

$$\frac{\|\boldsymbol{u}^{\delta}(\hat{t}) - \boldsymbol{u}(\hat{t})\|_{\ell^2}}{\|\boldsymbol{u}(\hat{t})\|_{\ell^2}} = \left(\frac{\sum_{n=1}^{N_{\text{eles}}}\sum_{p=1}^{P+1}\left|u^{\delta}_{n,p}(\hat{t}) - u_{n,p}(\hat{t})\right|^2}{\sum_{n=1}^{N_{\text{eles}}}\sum_{p=1}^{P+1}\left|u_{n,p}(\hat{t})\right|^2}\right)^{\frac{1}{2}}, \tag{57}$$

where $u^{\delta}_{n,p}(\hat{t})$ is the numerical solution in the nth element at the pth solution point. We also compute the L^2 functional norm of the relative error for comparison,

$$\frac{\|u^{\delta}(\hat{x},\hat{t}) - u(\hat{x},\hat{t})\|_{L^2}}{\|u(\hat{x},\hat{t})\|_{L^2}} = \left(\frac{\sum_{n=1}^{N_{\text{eles}}}\int_{\Omega_n}\left|u^{\delta}_n(\hat{x},\hat{t}) - u_n(\hat{x},\hat{t})\right|^2 d\Omega}{\sum_{n=1}^{N_{\text{eles}}}\int\Omega_n\left|u_n(\hat{x},\hat{t})\right|^2 d\Omega}\right)^{\frac{1}{2}}, \tag{58}$$

where the integral is approximated numerically using Gaussian quadrature with 12 quadrature points in each element.

We begin with the case of a well resolved Gaussian with $\sigma = 8/\sqrt{2\pi}$ and a solution polynomial of $P = 2$. Fig. 10, which plots the initial condition and the spectral weight distribution of this Gaussian, shows that the initial condition is indeed well resolved. Fig. 11 plots the relative error for different interface fluxes. As expected from the results in Fig. 5, the centered-centered scheme produces less error.

For the next case, the standard deviation of the Gaussian is decreased to $\sigma = 1/\sqrt{2\pi}$. Fig. 12 plots the initial condition and the spectral weight distribution for this Gaussian showing that the initial condition is now poorly resolved. Fig. 13 plots the relative error for different interface fluxes. Once again, as expected from the results in Fig. 5, the least amount of error is now exhibited by the center-one-sided scheme.

5.2. Case 2: 2D advection-diffusion of an approximate Gaussian

We now consider the 2D advection-diffusion equation in a periodic box. The domain is chosen to be square, $\hat{x}_1 \in [-10, 10]$, $\hat{x}_2 \in [-10, 10]$ and 2000 elements are used to construct a 2D, nonuniform, rectilinear grid with a minimum element size of $h_1 = 0.2$ and $h_2 = 0.1$ near the center of the domain as shown in Fig. 14. All cases have been verified to be stable when using the maximum stable time step estimate proposed in Eq. (43). We choose to use half of this estimate to minimize time integration errors.

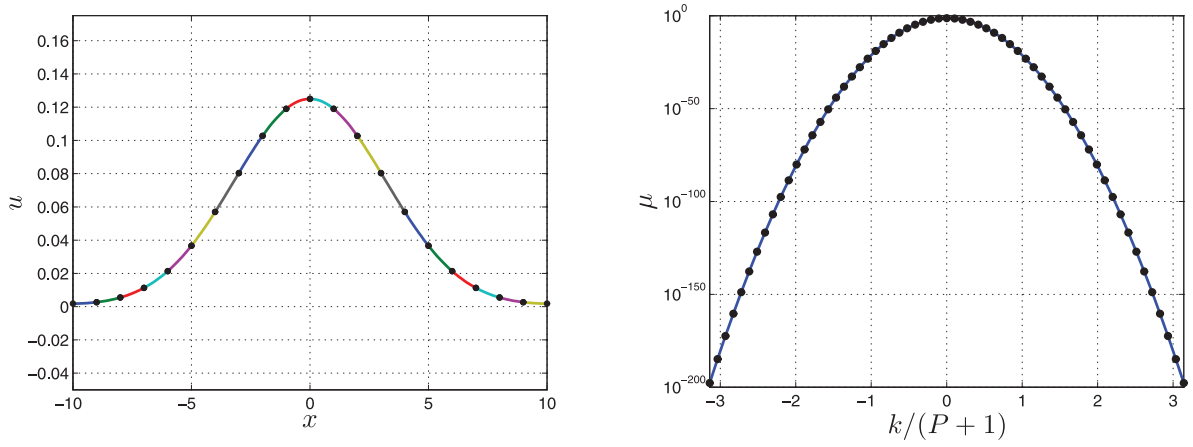

(a) Initial condition (b) Spectral weight distribution

Fig. 10. High resolution approximate Gaussian, $P = 2$, $\sigma = 8/\sqrt{2\pi}$.

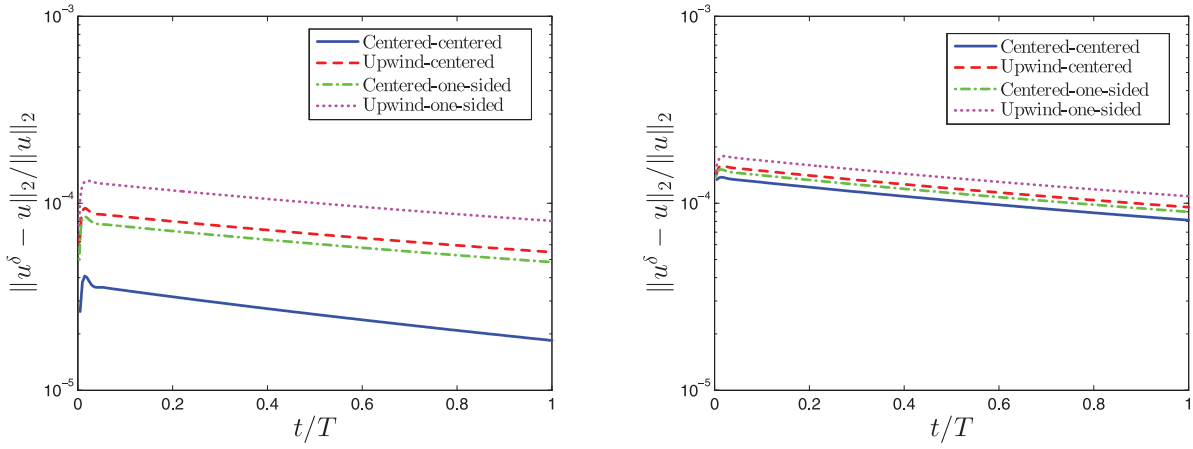

(a) ℓ^2 pointwise norm (b) L^2 functional norm

Fig. 11. Relative error vs. time periods for the RK44, DG scheme of order $P = 2$ using Gauss–Legendre solution points solving the advection-diffusion equation, $a = 10$, on a high resolution approximate Gaussian, $\sigma = 8/\sqrt{2\pi}$.

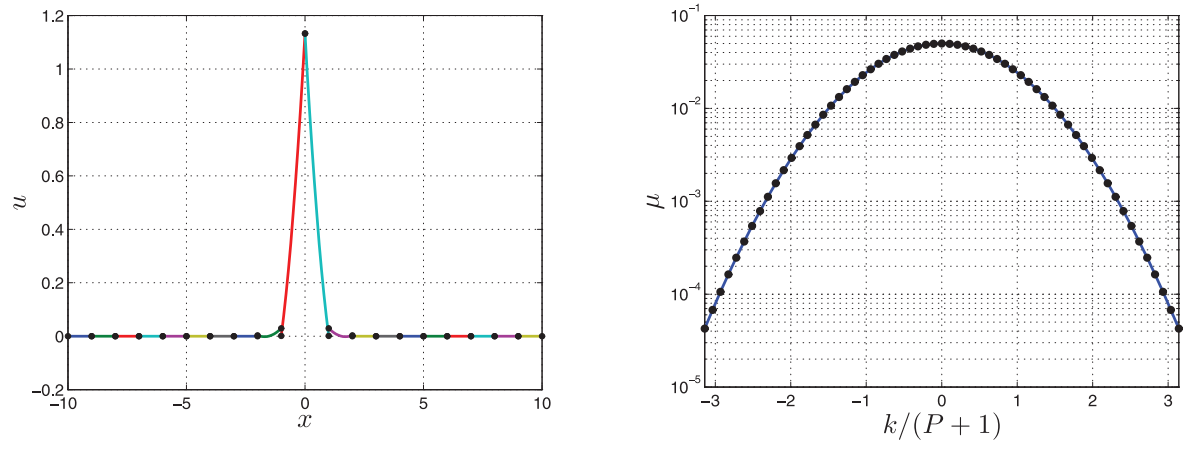

(a) Initial condition (b) Spectral weight distribution

Fig. 12. Low resolution approximate Gaussian, $P = 2$, $\sigma = 1/\sqrt{2\pi}$.

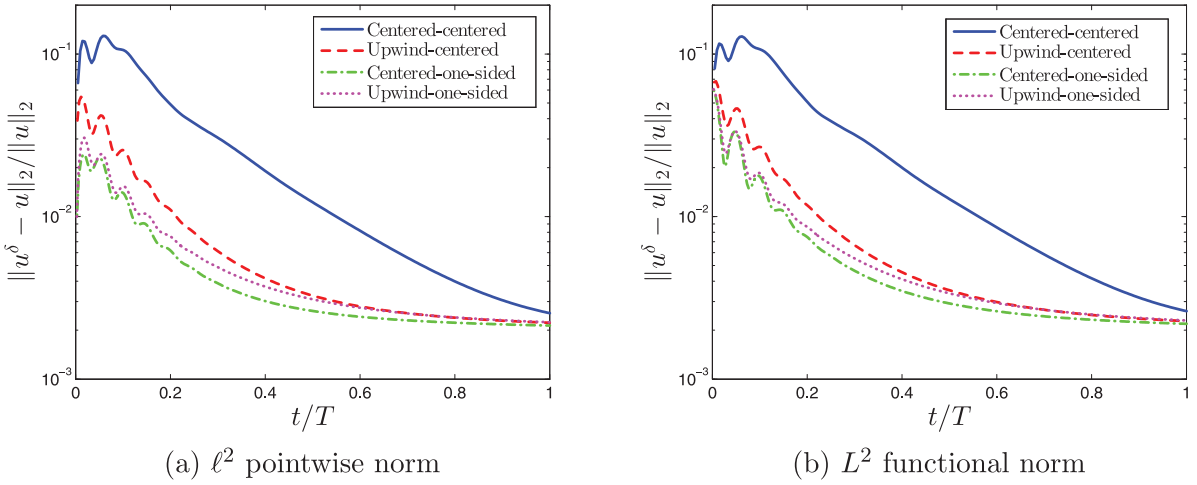

(a) ℓ^2 pointwise norm (b) L^2 functional norm

Fig. 13. Relative error vs. time periods for the RK44, DG scheme of order $P = 2$ using Gauss–Legendre solution points solving the advection-diffusion equation, $a = 10$, on a low resolution approximate Gaussian, $\sigma = 1/\sqrt{2\pi}$.

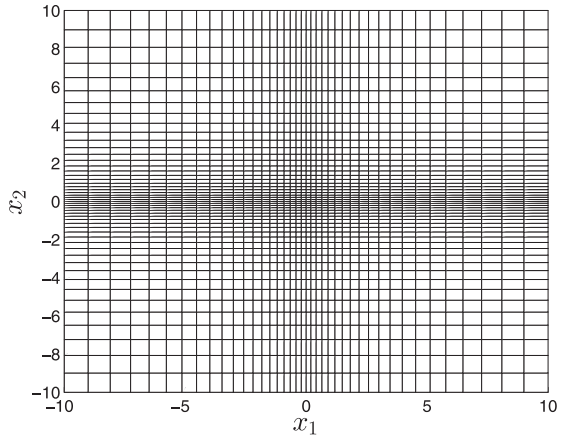

Fig. 14. Nonuniform rectilinear grid with 40 × 50 elements and a minimum element size of $h_1 = 0.2$ and $h_2 = 0.1$.

The initial condition and exact solution can be computed from,

$$u_{n,p}(\hat{t}) = \sum_{j_2=-N_{\hat{k}_2}}^{N_{\hat{k}_2}} \sum_{j_1=-N_{\hat{k}_1}}^{N_{\hat{k}_1}} \theta_{j_1,j_2} \prod_{d=1}^{2} \times \exp\left(-\left(\hat{b}\hat{k}_{d,j_d}^2 \hat{t}\right) \cos\left(\hat{k}_{d,j_d}\left(\hat{x}_{d,n,p} - \hat{a}_d \hat{t}\right)\right)\right), \tag{59}$$

where θ_{j_1,j_2} is defined as

$$\theta_{j_1,j_2} = \frac{\exp(-\sigma^2(\hat{k}_{1,j_1}^2 + \hat{k}_{2,j_2}^2)/2)}{2\pi\sigma \sum_{s_2=-N_{\hat{k}_2}}^{N_{\hat{k}_2}} \sum_{s_1=-N_{\hat{k}_1}}^{N_{\hat{k}_1}} \exp(-\sigma^2(\hat{k}_{1,j_1}^2 + \hat{k}_{2,j_2}^2)/2)}, \qquad \forall j_1, j_2. \tag{60}$$

The relative error is computed using Eq. (57).

The first case uses a well resolved Gaussian with $\sigma = 8/\sqrt{2\pi}$ and a solution polynomial of $P = 2$. Fig. 15 plots the initial condition and relative error for different interface fluxes. As in the 1D case, the centered-centered scheme produces the least amount of error.

The standard deviation of the Gaussian is now decreased to $\sigma = 1/\sqrt{2\pi}$ so that the initial condition is now under-resolved. Fig. 16 plots the initial condition and relative error for different interface fluxes. Since the grid is nonuniform, the Gaussian travels through a refined region during the first quarter period leading to smaller errors for the centered-centered and upwind-centered schemes. As the Gaussian travels through the less refined region near the half period, the centered-one-sided scheme starts producing the least amount of error resulting in the most accurate solution at the end of one period.

5.3. Case 3: 2D Couette flow

The last numerical test involves the solution of air passing between two parallel plates, separated by a distance H. The lower plate is kept stationary at a fixed temperature $T_l = 300K$ while the upper plate travels with constant velocity U_u and at a fixed temperature $T_u = 315K$. U_u is computed from a set Mach number of $\mathrm{Ma}_u = 0.2$. The Reynolds number of this flow is set to $\mathrm{Re}_u = 20$ and the dynamic viscosity, μ, is held constant. The ratio of specific heats, γ, and the Prandtl number, Pr, are set to 1.4 and 0.72, respectively. The domain is rectangular, $\hat{x}_1 \in [-1, 1]$, $\hat{x}_2 \in [0, 1]$, with periodic boundary conditions on the left and right boundaries and fixed and moving isothermal boundary conditions on the bottom and top boundaries, respectively. The flow field is initialized with the velocity of the top plate and RK44 is used to march the simulation to a steady state solution. The exact solution for the velocity profile is

$$u(\hat{\boldsymbol{x}}) = \frac{U_u \hat{x}_2}{H}, \qquad v(\hat{\boldsymbol{x}}) = 0. \tag{61}$$

A series of Cartesian and unstructured quadrilateral meshes are used to solve the Navier–Stokes equations. For example, Fig. 17 shows a (32 × 16) Cartesian mesh and a unstructured quadrilateral mesh with (639) elements along with the numerical Mach contours. For any given mesh, the nondimensional wavespeed, a, can be approximated by using Eq. (54) based on the properties of the flow attached to the upper plate,

$$a \approx \frac{\lambda_u h}{\nu_u} = \frac{(U_u + c_u)h}{\max\left(\frac{\mu}{\rho_u}, \frac{\gamma\mu}{\mathrm{Pr}\rho_u}\right)}. \tag{62}$$

For air, $\max\left(\frac{\mu}{\rho_u}, \frac{\gamma\mu}{\mathrm{Pr}\rho_u}\right) = \frac{\gamma\mu}{\mathrm{Pr}\rho_u}$. a can now be reduced by using the Reynolds number,

$$\mathrm{Re}_u = \frac{\rho_u U_u H}{\mu}, \tag{63}$$

$$a = \frac{\mathrm{Pe}_u(\mathrm{Ma}_u + 1)}{\gamma \mathrm{Ma}_u H} h, \tag{64}$$

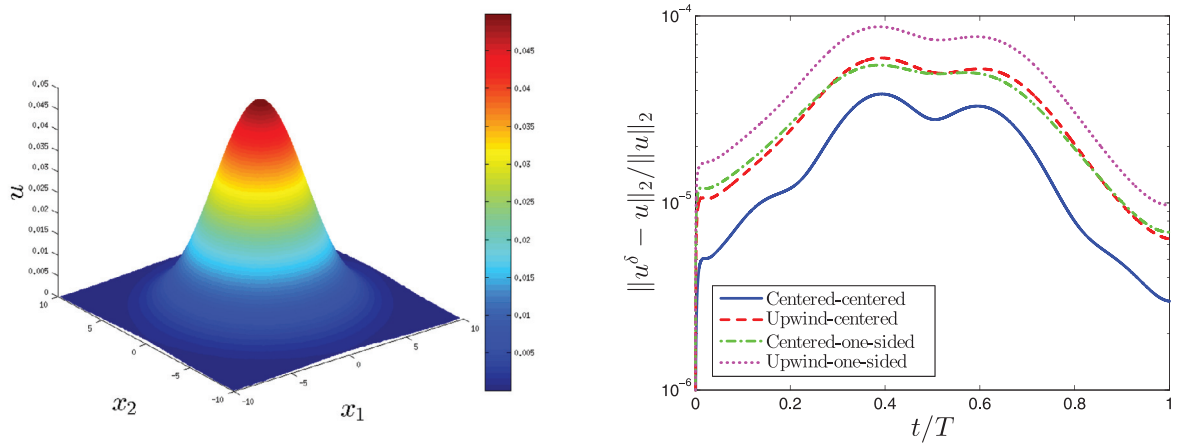

(a) Initial condition (b) ℓ^2 pointwise norm of relative error

Fig. 15. Initial condition and relative error for the RK44, DG scheme of order $P = 2$ using Gauss–Legendre solution points solving the advection-diffusion equation, $a = 10$, on a high resolution approximate Gaussian, $\sigma = 8/\sqrt{2\pi}$.

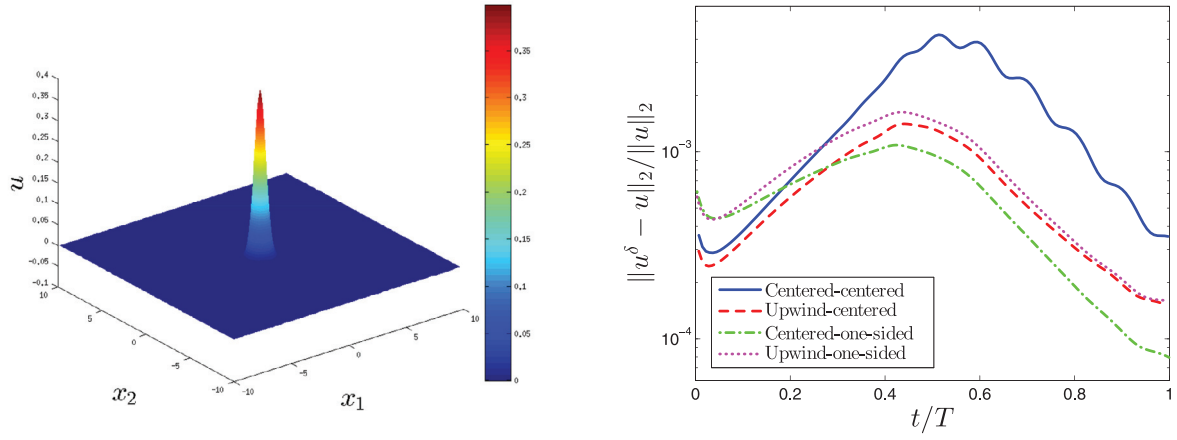

(a) Initial condition (b) ℓ^2 pointwise norm of relative error

Fig. 16. Initial condition and relative error for the RK44, DG scheme of order $P = 2$ using Gauss–Legendre solution points solving the advection-diffusion equation, $a = 10$, on a low resolution approximate Gaussian, $\sigma = 1/\sqrt{2\pi}$.

Table 4
Element size 'h' and nondimensional parameter 'a' for the meshes employed for Couette flow.

	N_{eles}					
	(4 × 2)	(8 × 4)	(16 × 8)	(32 × 16)	(159)	(639)
h	0.5	0.25	0.125	0.0625	0.07931	0.03956
a	30.86	15.43	7.714	3.857	4.894	2.441

where $\text{Pe}_u = \text{Re}_u\text{Pr} = 14.4$ is the Péclet number. For a given mesh, the element size h is computed as $h = \sqrt{\frac{2}{N_{\text{eles}}}}$ which recovers the exact element size for a Cartesian mesh. a is then computed for each mesh and shown in Table 4.

Convergence of the L^2 velocity error with grid spacing h is shown in Fig. 18 for $P = 2$ and Fig. 19 for $P = 3$. The rates of convergence for both Cartesian and unstructured meshes match well with the expected orders of around $P + 1$ [30].

The L^2 velocity errors and orders of accuracy are given in Table 5 for the Cartesian meshes and Table 6 for unstructured meshes. For $P = 2$, Cartesian meshes, the upwind-one-sided scheme produces less error for the less refined case while the upwind-centered scheme produces less error when the mesh is more refined. For $P = 3$, the upwind-one-sided scheme produces less error for all meshes which matches the results from Table 2. For unstructured meshes, the upwind-centered scheme produces less error for $P = 2$ and upwind-one-sided scheme produces less

Table 5
Couette flow results for the RK44, DG scheme using Gauss–Legendre solution points on Cartesian quadrilateral meshes.

		Upwind-centered			Upwind-one-sided		
P	N_{eles}	L^2 Error	Order	$\frac{\Delta\hat{t}_{\max}}{\Delta\hat{t}_{\text{pred}}}$	L^2 Error	Order	$\frac{\Delta\hat{t}_{\max}}{\Delta\hat{t}_{\text{pred}}}$
2	(4 × 2)	4.415e−05	–	1.3	4.358e−05	–	1.1
	(8 × 4)	5.256e−06	3.07	1.4	5.427e−06	3.01	1.0
	(16 × 8)	5.934e−07	3.15	1.5	6.430e−07	3.08	1.0
	(32 × 16)	6.546e−08	3.18	1.3	7.741e−08	3.05	1.0
3	(4 × 2)	4.584e−07	–	1.3	4.380e−07	–	1.1
	(8 × 4)	3.089e−08	3.89	1.4	2.706e−08	4.02	1.0
	(16 × 8)	1.995e−09	3.95	1.2	1.622e−09	4.06	1.0
	(32 × 16)	1.274e−10	3.97	1.1	1.004e−10	4.01	1.0

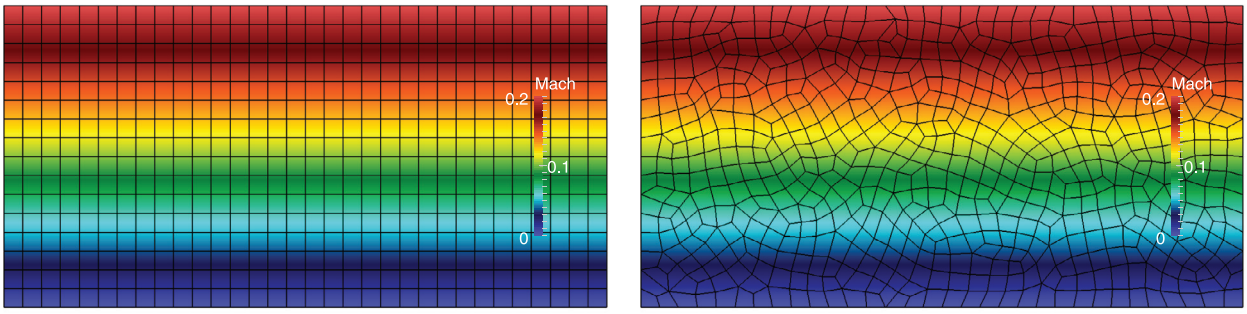

(a) Cartesian mesh, (32×16) elements (b) Unstructured mesh, (639) elements

Fig. 17. Couette flow Mach contours, DG upwind-one-sided scheme using Gauss–Legendre solution points, $P = 3$.

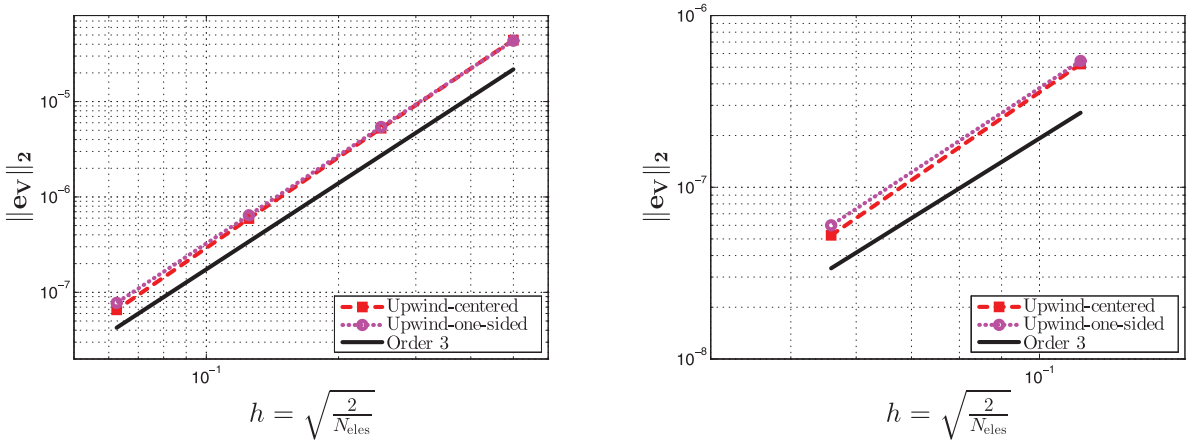

(a) Cartesian meshes (b) Unstructured quadrilateral meshes

Fig. 18. 3rd order results for Couette flow, RK44, DG scheme using Gauss–Legendre solution points, $P = 2$.

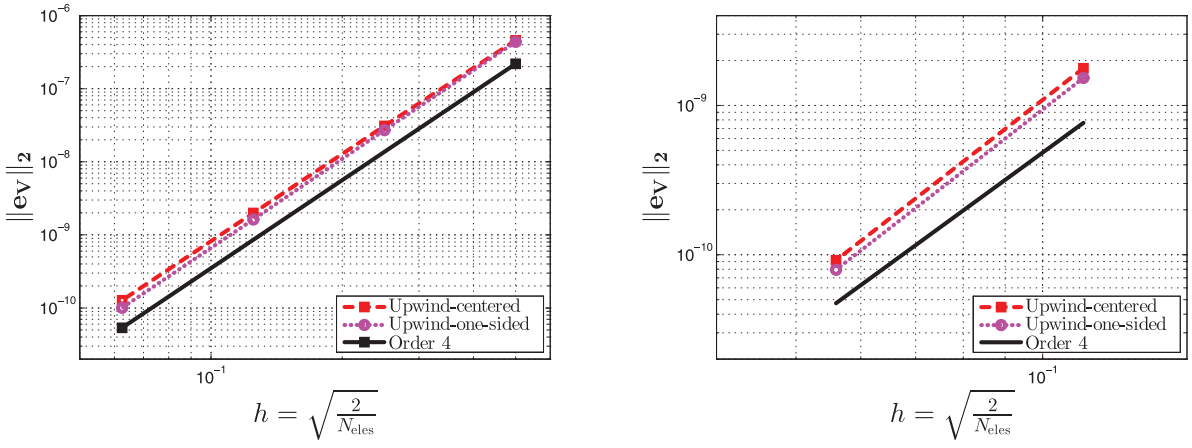

(a) Cartesian meshes (b) Unstructured quadrilateral meshes

Fig. 19. 4th order results for Couette flow, RK44, DG scheme using Gauss–Legendre solution points, $P = 3$.

error for $P = 3$. This matches well with the results from the Cartesian meshes since the meshes are more refined.

The ratios of maximum allowable time step over the estimated time step computed using Eq. (47), $\frac{\Delta \hat{f}_{max}}{\Delta \hat{f}_{pred}}$, are shown in Table 5 for the Cartesian meshes. The results show that the time step estimate remains conservative for both schemes and matches almost exactly for the upwind-one-sided scheme as was expected from Fig. 8. It's also important to note that in the case of the upwind-centered scheme, the time step estimate loses accuracy near $a \approx 10$, as expected from Fig. 8.

The results from the unstructured meshes in Table 6 show that the time step estimate is conservative for the upwind-centered scheme but not for the upwind-one-sided scheme, however, the time step estimate is still fairly accurate for both cases.

Table 6
Couette flow results for the RK44, DG scheme using Gauss–Legendre solution points on unstructured quadrilateral meshes.

		Upwind-centered			Upwind-one-sided		
P	N_{eles}	L^2 Error	Order	$\frac{\Delta \hat{t}_{max}}{\Delta \hat{t}_{pred}}$	L^2 Error	Order	$\frac{\Delta \hat{t}_{max}}{\Delta \hat{t}_{pred}}$
2	(159)	5.214e−07	–	1.5	5.432e−07	–	0.9
	(639)	5.249e−08	3.31	1.4	6.003e−08	3.18	0.9
3	(159)	1.777e−09	–	1.3	1.529e−09	–	0.8
	(639)	9.192e−11	4.27	1.3	7.922e−11	4.27	0.8

6. Conclusion

In this paper, Fourier analysis is performed for the FR formulation for the linear advection-diffusion equation. In our analysis, we have focused on different interface flux formulations of the nodal DG scheme on Gauss–Legendre points although the same technique can be applied to any scheme within the FR formulation. The contributions of this study can be split into two main results. First, we have provided a maximum stable time step estimate for the linear advection-diffusion and Navier–Stokes equations on unstructured, tensor product elements. The estimates are accurate within 50% error on all test cases and are conservative on tests with Cartesian grids but not always on unstructured grids. Second, we presented both theoretical and numerical verification that schemes with centered values produce less error for well resolved solutions while schemes with one-sided values produce less error for solutions that are under-resolved.

Acknowledgments

This work was supported under the National Science Foundation Graduate Research Fellowships Program, the Stanford Graduate Fellowship program and the Air Force Office of Scientific Research (Grant FA9550-14-1-0186).

References

[1] Reed W. H., Hill T. Triangular mesh methods for the neutron transport equation. Los Alamos Report LA-UR-73-4791973.
[2] Cockburn B, Karniadakis GE, Shu C-W. The development of discontinuous Galerkin methods. Springer; 2000.
[3] Hesthaven JS, Warburton T. Nodal discontinuous Galerkin methods: algorithms, analysis, and applications, vol. 54. Springer Science & Business Media; 2007.
[4] Kopriva DA, Kolias JH. A conservative staggered-grid Chebyshev multidomain method for compressible flow. Tech. Rep. DTIC Document; 1995.
[5] Liu Y, Vinokur M, Wang Z. Spectral difference method for unstructured grids I: basic formulation. J Comput Phys 2006;216(2):780–801.
[6] Huynh H. A flux reconstruction approach to high-order schemes including discontinuous Galerkin methods. AIAA Paper 2007;4079:2007.
[7] Huynh HT. A reconstruction approach to high-order schemes including discontinuous Galerkin for diffusion. AIAA Paper 2009;403:2009.
[8] Vincent PE, Castonguay P, Jameson A. A new class of high-order energy stable flux reconstruction schemes. J Sci Comput 2011;47(1):50–72.
[9] Jameson A, Vincent PE, Castonguay P. On the non-linear stability of flux reconstruction schemes. J Sci Comput 2012;50(2):434–45.
[10] Asthana K, López-Morales MR, Jameson A. Non-linear stabilization of high-order flux reconstruction schemes via fourier-spectral filtering. J Comput Phys 2015;303:269–94.
[11] Castonguay P, Vincent PE, Jameson A. A new class of high-order energy stable flux reconstruction schemes for triangular elements. J Sci Comput 2012;51(1):224–56.
[12] Williams D, Castonguay P, Vincent PE, Jameson A. Energy stable flux reconstruction schemes for advection–diffusion problems on triangles. J Comput Phys 2013;250:53–76.
[13] Williams D, Jameson A. Energy stable flux reconstruction schemes for advection–diffusion problems on tetrahedra. J Sci Comput 2014;59(3):721–59.
[14] Gao H, Wang Z. A conservative correction procedure via reconstruction formulation with the chain-rule divergence evaluation. J Comput Phys 2013;232(1):7–13.
[15] Wang Z, Gao H. A unifying lifting collocation penalty formulation including the discontinuous Galerkin, spectral volume/difference methods for conservation laws on mixed grids. J Comput Phys 2009;228(21):8161–86.
[16] Hu FQ, Hussaini M, Rasetarinera P. An analysis of the discontinuous Galerkin method for wave propagation problems. J Comput Phys 1999;151(2):921–46.
[17] Moura R, Sherwin S, Peiró J. Linear dispersion–diffusion analysis and its application to under-resolved turbulence simulations using discontinuous galerkin spectral/hp methods. J Comput Phys 2015;298:695–710.
[18] Ainsworth M. Dispersive and dissipative behaviour of high order discontinuous Galerkin finite element methods. J Comput Phys 2004;198(1):106–30.
[19] Toulorge T, Desmet W. Cfl conditions for Runge–Kutta discontinuous Galerkin methods on triangular grids. J Comput Phys 2011;230(12):4657–78.
[20] Vincent PE, Castonguay P, Jameson A. Insights from von Neumann analysis of high-order flux reconstruction schemes. J Comput Phys 2011;230(22):8134–54.
[21] Asthana K, Jameson A. High-order flux reconstruction schemes with minimal dispersion and dissipation. J Sci Comput 2014;62(3):913–44.
[22] Asthana K. Analysis and design of optimal discontinous finite element schemes. Stanford University; 2016. Ph.D. thesis.
[23] Bassi F, Rebay S. A high-order accurate discontinuous finite element method for the numerical solution of the compressible Navier–Stokes equations. J Comput Phys 1997;131(2):267–79.
[24] Cockburn B, Shu C-W. The local discontinuous Galerkin method for time-dependent convection-diffusion systems. SIAM J Numer Anal 1998;35(6):2440–63.
[25] Cockburn B, Dong B. An analysis of the minimal dissipation local discontinuous Galerkin method for convection–diffusion problems. J Sci Comput 2007;32(2):233–62.
[26] Lele SK. Compact finite difference schemes with spectral-like resolution. J Comput Phys 1992;103(1):16–42.
[27] MacCormack RW. A numerical method for solving the equations of compressible viscous flow. AIAA J 1982;20(9):1275–81.
[28] MacCormack RW. Current status of numerical solutions of the navier-stokes equations. AIAA Paper 1985;32:1985.
[29] Castonguay P. High-order energy stable flux reconstruction schemes for fluid flow simulations on unstructured grids. Stanford University; 2012. Ph.D. thesis.
[30] Williams DM. Energy stable high-order methods for simulating unsteady, viscous, compressible flows on unstructured grids. Stanford University; 2013. Ph.D. thesis.